Supporting Information

Taylor *et al.* 10.1073/pnas.0813416106

SI Text

Methods. ***Fabrication protocol.*** Devices were made by using multilayer soft lithography in which consecutive replica molding and bonding steps are used to realize monolithic multilayer devices. Photolithography masks were designed by using AutoCAD software (Autodesk) and used to generate high-resolution (20,000 dpi) transparency masks (CAD/Art Services). Molds were fabricated by photolithography on 10.2 cm silicon wafers (Silicon Quest International). The flow layer consisted of two different channel profiles: 3.5-μm-high rectangular trapping channels allowing for sieve valving, and 12-μm-high rounded channels used for standard flow. The 3.5-μm layer was made with SU8-5 negative photoresist (Microchem Corp.), and the 12-μm rounded layer was made with SPR220-7 positive photoresist (Microchem Corp.). The control master was a single layer mold consisting of 25-μm-high squared features made with SU8-2025 negative photoresist (Microchem Corp.). Resist processing was performed according to the manufacturer's specifications.

Microfluidic control. Microfluidic operation was fully computer-controlled, excluding cell loading and trapping. Custom software was designed and executed in LabVIEW (National Instruments). Microfluidic valves were actuated by using high-speed computer-controlled solenoid micropump manifolds (Fluidigm) via a PCI-6533 digital input/output card (National Instruments). A single LabVIEW program operated all experiment types, with user-designed experiments inputted as parsed text files. Scheduling algorithms were included to maximize the frequency of experiment refresh of all 32 chemical sequences.

Chemicals and media. Yeast cells were grown with aeration overnight in YPD (30 degrees Celcius), diluted, and grown to log phase in synthetic complete dextrose (SCD) on the day of the experiment. BSA (20 mg/mL) was added to all SCD solutions to act as an antifouling agent. We found that this helped to avoid adherence of yeast cells to polydimetnylsiloxane (PDMS) walls and reduced nonspecific binding of the α-factor to the PDMS or tubing walls (1). α-Factor was purchased from ZymoResearch.

Cell preparation. Cells were diluted from overnight culture into fresh SCD and grown to log phase. To improve uniform cell loading, the cell solution was sonicated at low power, causing the dissociation of cell clumps. To achieve ideal seeding density, cells were concentrated to an A_{600} of 3 immediately before loading. This allowed for a seeding density of $\approx$2–5 cells per microchamber, and with 8 microchambers per experiment, $\approx$20–30 initial cells per experiment. Once loaded onto the microfluidic device, the cells were perfused with fresh SCD for at least 2 h before the initial α-factor stimulation. Image acquisition was started at least 1 h before α-factor stimulation to record basal fluorescence level and initial cell number. Cells were grown and stimulated at room temperature.

Chemical mixing and perfusion. Between every exchange or refreshing of medium, the following refresh protocol was used:

1. Prime and wash multiplexer. Perfuse adjacent waste row with chemical solution for 20 s.
2. Refresh microchambers. Perfuse experiment row with chemical solution for 70 s.
3. Wait. A wait of 3 s is used to dissipate pressure buildup that occurs across the high-impedance microchamber traps. This protocol allowed us to refresh an experimental row fully approximately every 100 s.

Constant stimulation protocol. Yeast strains were stimulated continuously with 32 exponentially distributed α-factor concentrations ranging from 0 to 100 nM beginning at $t = 0$ s. α-Factor concentrations were calculated as: α-factor concentration = 1.16^i nM; where i = row number. The calculated concentrations were then rounded to account for discrete ratio mixing. The first row (row index 0) was used as a negative control (α-factor = 0 nM). All 32 α-factor concentrations were created on a chip by using ratio mixing enabled by the peristaltic pump. Mixing protocols are found in Table S1. Each chemical mixture protocol was based on a 10-pump cycle period. To administer a particular mixture continually, the 10-pump cycle was repeated.

Mixing of pumped solutions occurred through mechanisms of Taylor dispersion (2). We tested the mixing in our chip by creating a concentration gradient of fluorescent dye (fluorescein). The effective concentration was measured by taking a fluorescent intensity measurement of the dye as it passed the entrance of an experiment row. A plot of measured fluorescence intensity vs. relative concentrations is shown in Fig. 2*E*. The results show good agreement, indicating that our solutions are well mixed and our concentration profiles are precise.

Single-transient pulse protocol. Scheduling of the single-pulse experiment is shown in Fig. S4*A*. Protocols of the same concentration were grouped together to allow for the simultaneous refreshing of multiple experiment rows. Concentration groups were staggered by 2.5 min. Approximately 16 p.s.i. (110.3 kPa) was applied to the different chemical lines.

Short repeated-pulses protocol. Scheduling of the repeated-pulse experiment is shown in Fig. S4*B*. Concentration groups were staggered by 2.5 min. Approximately 16 p.s.i. (110.3 kPa) was applied to the different chemical lines.

Biological constructs. The full list of strains is given in Table S2. Deletion mutants were obtained from the Open Biosystems Yeast Knockout (YKO) collection, as was the wild- type (WT) BY4714 strain. All strains are derived from the parental S288C strain and have the base genotype MATa *his3*Δ*1 leu2*Δ*0 met15*Δ*0 ura3*Δ*0*. Deletion mutants in the YKO collection were derived by using a PCR-based strategy to replace the ORF with a KanMX deletion cassette. We confirmed each deletion by using PCR methods. To report on mating pathway-dependent gene expression, we transformed the strains with the gene coding for enhanced green fluorescent protein (GFP) under control of a mating-specific promoter. The promoter consisted of three consecutive pheromone response elements (PREs) from the PRM1 promoter, plus three flanking PRM1 promoter bases on each side, plus a CYC1 core promoter placed just before the ATG start site. The PRE-promoter-GFP construct (PRE-GFP) was placed adjacent to the *HIS3* selection element by using the Longtine *et al.* cassettes (3) and integrated at the *his3*Δ*1* locus by using flanking sequences introduced by long-oligonucleotide PCR. The integration was verified by PCR. In each strain, the pheromone protease gene, *BAR1*, was deleted to preclude complications resulting from genotype-dependent Bar1 activity. The *BAR1* coding sequence was deleted by using PCR methods with the pFA6a-hphNTI hygromycin cassette as described by Janke *et al.* (4).

Image analysis pipeline algorithms. Each set of microfluidic cell traps was acquired in two fields of view, giving a total of 256 experiment traps $\times$ 2 = 512 differential interference contrast/fluorescent image pairs acquired per time point. We acquired a full set of images every 15 min, which was slightly longer than the time it took to iterate over and acquire the 512 image pairs. Over

a 12.5-h experiment, this procedure resulted in >50,000 images (≈120 Gb of image data). To process data, a customized image analysis pipeline was developed by using MATLAB software (Mathworks).

Central to our image analysis pipeline were algorithms for automated cell segmentation and enhanced GFP concentration calculation. These algorithms consisted of the three major steps described below.

Identification of microfluidic region of interest. Before cell segmentation, the images were cropped to exclude the non-yeast-containing regions outside of the cell flow channels. This reduced computational time and false-positives caused by out-of-channel segmentation. To detect the channel boundaries, the detection algorithms took advantage of (*i*) the horizontal orientation of the yeast flow channels and (*ii*) the dark illumination of channel edges. The horizontal projection of the image, calculated by summing each image column, resulted in a 1D signal in which four sharp local minima represented the four channel edges. The projected values were then normalized to the range [0, 1] and the local minima were detected by thresholding.

The edge detection algorithm was an iterative procedure that used the a priori knowledge that there should be two channels whose approximate width and separation from each other (in pixels) were known. The threshold was at first set to a user-defined initial value. If thresholding found two local minima whose distance from each other was <50 pixels, only the one whose value was smaller was kept. If this procedure detected four local minima, these local minima were kept as the channel edges. If fewer than four local minima were found, the procedure was repeated with the threshold incremented by 0.01 (a.u.); and if more than four local minima were found, the procedure was repeated with the threshold decremented by 0.01. If the procedure failed to converge to four local minima, channel detection failed, and cell segmentation was performed on the whole image. Fig. S3*B* shows the detected channel edges overlaid in red on the differential interference contrast (DIC) image.

Cell segmentation. After channel detection, the DIC image was enhanced by using background subtraction. The background was estimated by spatially averaging the image by using a 21 × 21 mean filter. The resultant image is shown in Fig. S3*C*.

The first step in cell segmentation identified the cell walls. Yeast cell walls were clearly visible as continuous borders that were darker than the background, giving two useful properties: the local mean was low, and the local variance was high. Cell wall pixels were marked as those pixels whose local mean was below a threshold T_m and whose variance was above a threshold T_v (5). A 5 × 5 neighborhood was used to calculate the local mean and variance. The threshold T_m was set to $\mu_m - (1/2)\,\sigma_m$, where the μ_m and σ_m were the global mean and SD of the local mean image, respectively. Similarly, the threshold T_v was set to $\mu_v + (1/3)\,\sigma_v$, where the μ_v and σ_v were the global mean and SD of the local variance image, respectively. The cell wall segmentation result is shown in Fig. S3*D*.

This segmentation result has both false-negatives and false-positives (apparent discontinuities in cell walls and noncell wall pixels detected as cell wall pixels, respectively), and further processing was required. First, small holes inside the detected cell walls were removed by a morphological closing with a 5 × 5 structuring element. Second, detected channel edges were removed by assigning to zero each row of pixels five pixels above and below the detected channel edges followed by hysteresis thresholding (6). The result is shown in Fig. S3*E*. Typically some parts of the channel edges were still falsely detected as cell wall pixels, but these pixels were removed in the subsequent processing steps.

The image with the detected cell walls was used to obtain a mask of cell areas. First, the image was dilated by a circular structuring element inside a 11 × 11 square. After, holes inside the objects were filled, and the image was subsequently eroded by the same circular structuring element. The result is shown in Fig. S3*F*. The detected cell walls were then removed from the mask (Fig. S3*G*). Because of noise in cell wall detection, some cells were incorrectly grouped together and recognized as a single cell. These were separated from each other with the watershed of the Euclidean distance function of the complement image (7). The *h*-maxima transformation was used to prevent oversegmentation. Finally, objects that were smaller than 80 pixels in size were excluded. The final cell segmentation result is shown in Fig. S3*H*.

Measurement of GFP concentration. GFP concentration values were calculated from the fluorescent channel images. Average background florescence, as calculated by the mean fluorescence of values outside of the segmented cells, was first subtracted from each pixel value. Total fluorescence of each cell was then summed from the image pixel values bounded by the segmented regions identified from the segmentation algorithms. For each cell, the GFP concentration was obtained by dividing the total cellular fluorescence intensity by a volume estimate for the cell. The volume estimate was based on the cross-sectional cell area that was obtained from the cell segmentation result and calculated by using the "conical" method as described in ref. 8.

Results. ***Experimental variability of microfluidic platform.*** Experimental variability is caused by condition differences between experiments within a single device and between experiments taken on different devices on different days. Sources of in-chip variability include precision limits of chemical mixing, consistency of media conditions across experimental positions, and variations in *z*-position. To maximize chemical mixture precision we used on-chip pumping and mixing of α-factor stock solutions to create precise final stimulant concentrations (demonstrated in Fig. 2*E* and discussed in the main text). To ensure reproducibility across experimental positions (different columns of the microfluidic device), we used FITC and food dye tracers to determine the perfusion time needed to replace reliably the well-mixed media solutions across a row of microchambers (30 s). During experimentation we used a much longer refresh time (70 s) to exchange the media robustly. We empirically characterized in-chip reproducibility by stimulating eight identical yeast genotypes (WT) with a series of constant α-factor concentrations (Fig. S5). We find that variability is minimal (<10–20%) and not dependent on column position. To reduce variability caused by image focus, we manually defined focus positions for all images before image acquisition and programmed our microscope to return to these positions at each time point. We found that this method was robust, and long-time courses could be obtained with minimal focus drift (Fig. S2). In addition, we used a 40× long distance objective (NA = 0.6) with a depth of field (estimated 1.5 μM) similar to the diameter of yeast cells. This increased the robustness of the fluorescent measurement, which was advantageous over a higher magnification and numerical aperture objectives.

Variability across experiments taken with different chips on different days is primarily caused by precision limitations of stock α-factor solutions and day-to-day fluctuations in fluorescent excitation intensity. Quantitative comparisons between genotypes were possible by internally controlling all measurement by normalizing response to a WT control. In each experiment, we reserved one column per chip (chosen randomly) for WT, and mutant responses were analyzed after normalization to WT.

Finally, we found that variability in population-averaged statistics (e.g., mean response) increased when initial seeding density was low because of sampling error of the biological response. An initial density of 20–30 cells (2.5–3.75 cells per microchamber) greatly reduced this source of error, and we

conducted our experiments in this regime. Increases in chamber size will further address issue, and technical modifications to the trapping scheme are in development.

Morphology classifications under constant stimulation. Throughout our experiments we found α-factor concentration-dependent morphological responses. This was most apparent when the cells were subjected to continuous stimulation for long times under chemostatic conditions. In our work, we classified the morphologies after 6 h of constant α-factor stimulation by using three general morphology types

1. Budding yeast.

Yeast cells maintained their vegetative rounded shape seen for exponentially growing cells. At the lowest concentrations these cells did not cell cycle arrest ($<$5 nM).

2. Elongated.

Elongated cells demonstrated rod-shaped phenotypes. The degree of elongation varied, and at long time scales ($>$14 h) we observed cells with major axes $>5\times$ minor axis. Elongated morphologies were observed at intermediate α-factor concentrations (4–20 nM).

3. Shmooing.

Shmooing cells were rounded with small sharp protrusions and cell cycle arrest. These cells were mostly observed at higher α-factor concentrations ($>$20 nM).

Fig. S6 demonstrates morphology analysis of each strain across all α-factor concentrations taken at 6 h after initial stimulation. The concentration range for each morphology varied drastically among some mutants. Some mutants like *far1*D only showed the budding yeast morphology and lacked any other type. Others such as *msg5*D and *ptp2*D displayed an extended shmoo concentration range (extending to $<$4 nM) compared with WT.

Single-pulse analysis. To investigate the pulse width-dependence of the rate of pathway deactivation, we quantitatively examined the kinetics of pathway shutdown after α-factor release in multiple ways. First, we measured the delay between α-factor release and time to reach maximal GFP concentration across all pulse widths (Fig. S7*A*). We find that this time was independent of pulse width, occurring $\approx$30 min after release from α-factor stimulation for all conditions. Second, we measured GFP decay rates upon α-factor release by fitting the postmaximum GFP time course data to a model of exponential decay. Across replicates ($n = 3$) and across all conditions giving significant GFP expression (all combinations of 50 and 20 nM $\times$ 60, 90, 120, 150, 180, and 210 min), we found a condition-independent decay rate of 0.0046 ± 0.0014 min^{-1}. Third, we compared the integrated GFP response to total integrated input dose. Because we know that the activation rate for a given α-factor concentration is constant, as is the time to initiate deactivation upon release, deactivation rates that are independent of pulse width should map linearly to input dosage. We in fact observed this relationship (Fig. S7*B*). Taken together, these results indicate that for the pulse widths tested, we do not measure network adaptation effects resulting in increased or decreased rate of pathway shutdown.

Pulse width-dependent growth rate. Manual counts of numbers of cells across time were used to obtain exact cell growth curves. Fig. S7*C* gives the growth curves for WT cells across all single-pulse widths of the 50 nM concentration. Cell cycle arrest is observed $\approx$75 min after stimulation and persists approximately for a duration equivalent to the pulse width. We were unable to detect any arrest for the $\leq$20 nM conditions.

Calculation of d[GFP]/dt. Initial rate of GFP molecule production (d[GFP]/dt) was calculated as the slope of the line fitted to the population averaged GFP response for $t = 30$ min to $t = 180$ min. This time interval was chosen to allow for GFP maturation and to end before response saturation. We found that yeast cells demonstrated an α-factor concentration-dependent rate of GFP expression.

1. Colman-Lerner A, *et al.* (2005) Regulated cell-to-cell variation in a cell fate decision system. *Nature* 437:699–706.
2. Squires TM (2005) Microfluidics: Fluid physics at the nanoliter scale. *Rev Modern Phys* 77:977–1026.
3. Longtine MS, *et al.* (1998) Additional modules for versatile and economical PCR-based gene deletion and modification in *Saccharomyces cerevisiae*. *Yeast* 14:953–961.
4. Janke C, *et al.* (2004) A versatile toolbox for PCR-based tagging of yeast genes: New fluorescent proteins, more markers and promoter substitution cassettes. *Yeast* 21:947–962.
5. Niemisto A, *et al.* (2007) Computational methods for estimation of cell cycle phase distributions of yeast cells. *EURASIP J Bioinform Syst Biol* 46150.
6. Canny JF (1986)A computational approach to edge detection. *IEEE Trans Pattern Anal Machine Intell* 8:679–698.
7. Soille P (2003) *Morphological Image Analysis: Principles and Applications* (Springer, Heidelberg, Germany).
8. Gordon A, *et al.* (2007) Single-cell quantification of molecules and rates using open-source microscope-based cytometry. *Nat Methods* 4:175–181.

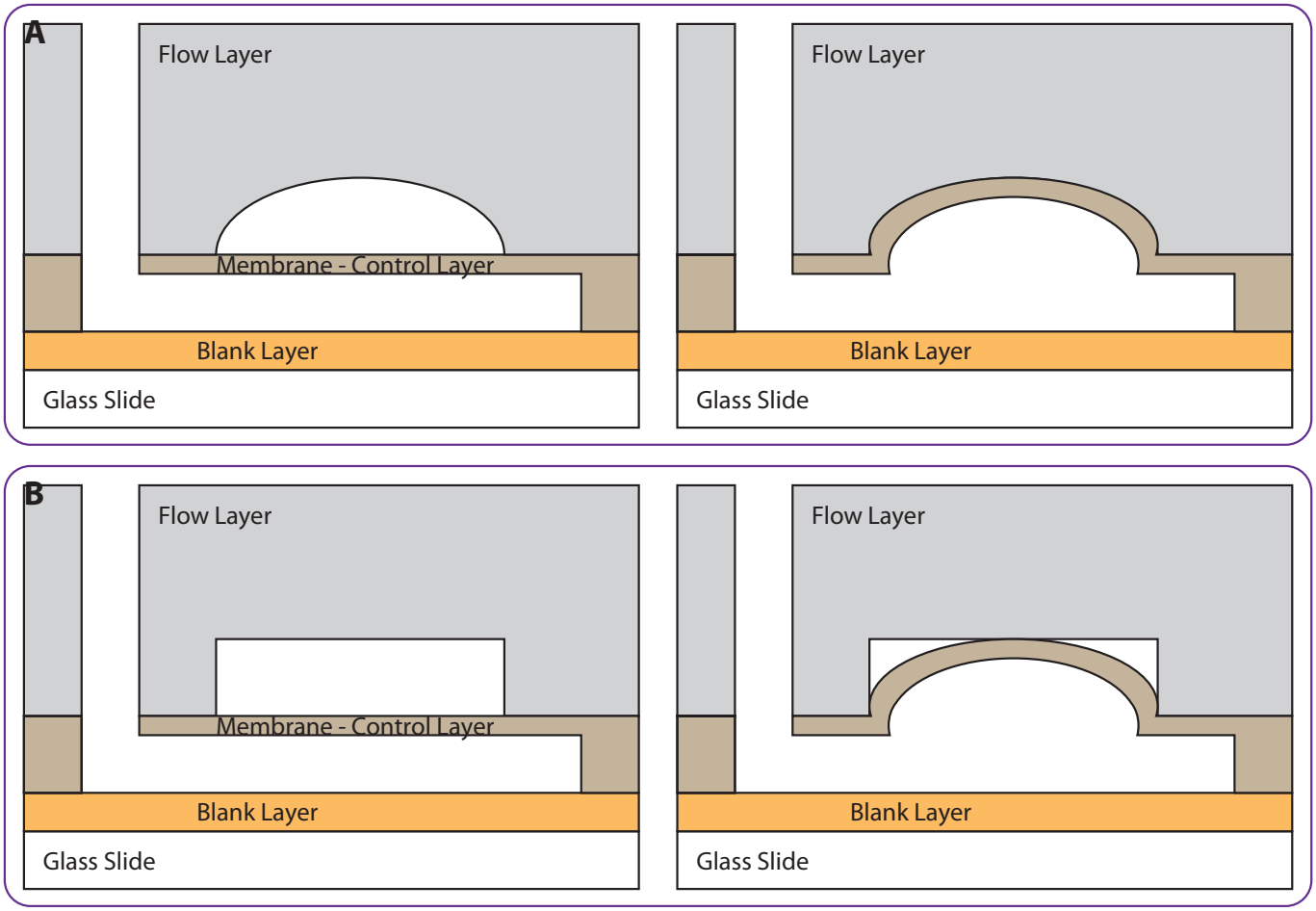

Fig. S1. Cell trapping. (*A*) Standard MSL valves deflect the elastomer membrane into a rounded flow channel, causing complete closure. (*B*) Sieve valves deflect the elastomer membrane into a rectangular flow channel, causing incomplete closure.

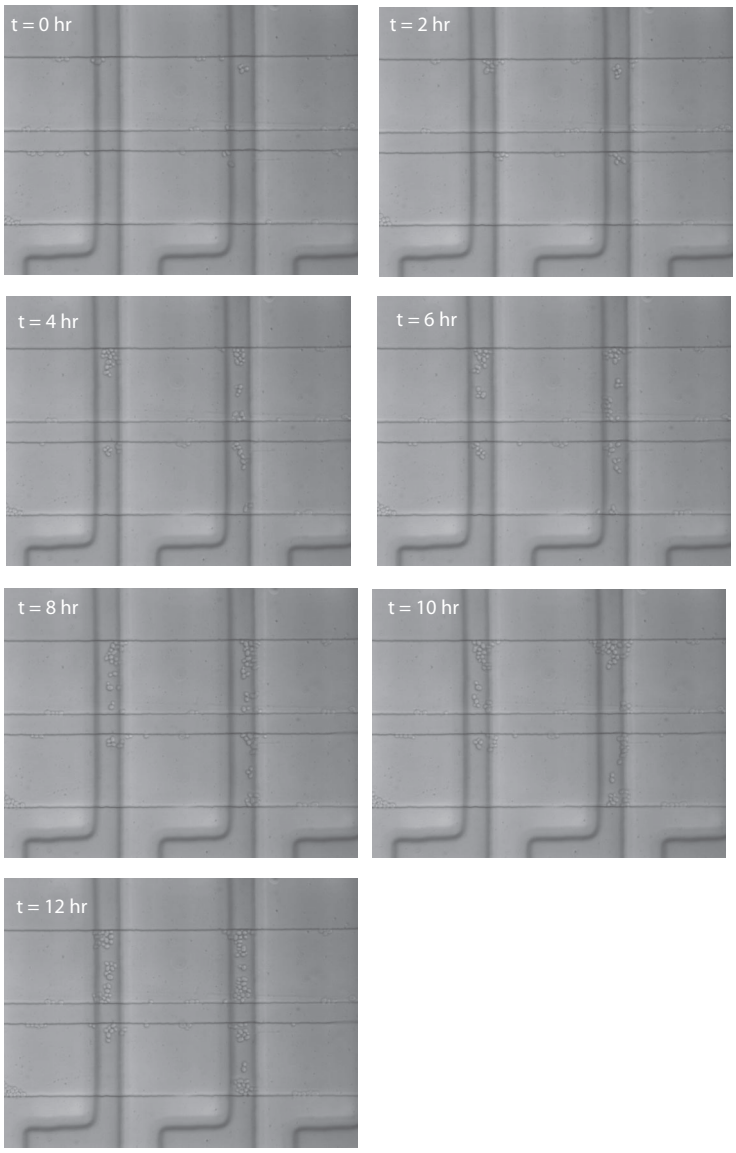

Fig. S2. Image focus over 12 h. Representative DIC images yeast cells taken over a 12-h time course are shown. By using an automated XYZ positioning, images were acquired at each position of the microfluidic device (256 microchambers × 2 fields of view per microchamber = 512 positions) every 15 min for 12 h (52 images). Shown here are the 2-h time points for a single position.

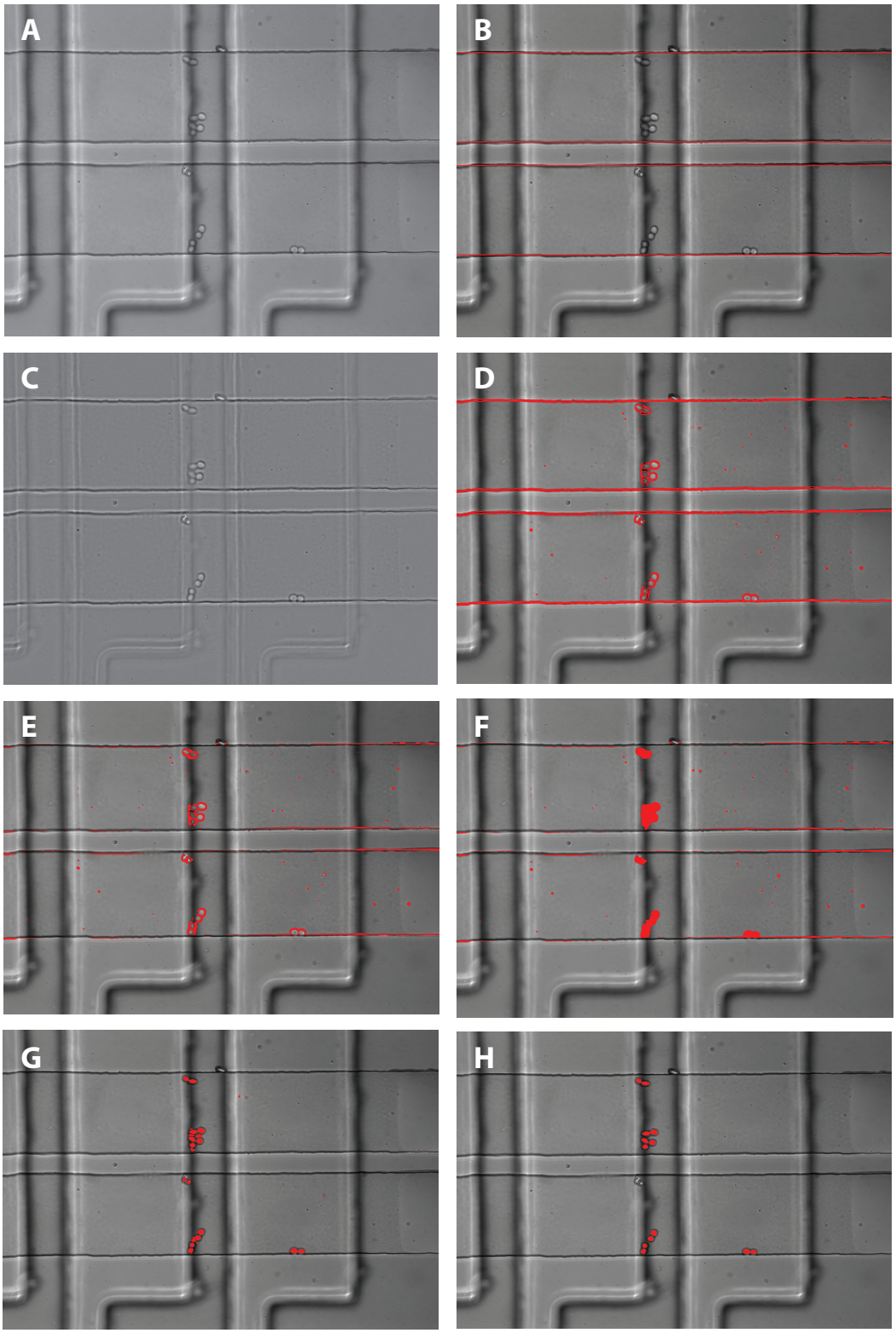

Fig. S3. Image segmentation algorithms. (*A*) Original cell image. (*B*) Microfluidic channel detection. (*C*) Enhanced brightfield image. (*D*) Yeast cell wall segmentation. (*E*) Cell wall segmentation after removal of channel edges. (*F*) Cell area mask. (*G*) Cell segmentation before postprocessing steps. (*H*) Final cell segmentation.

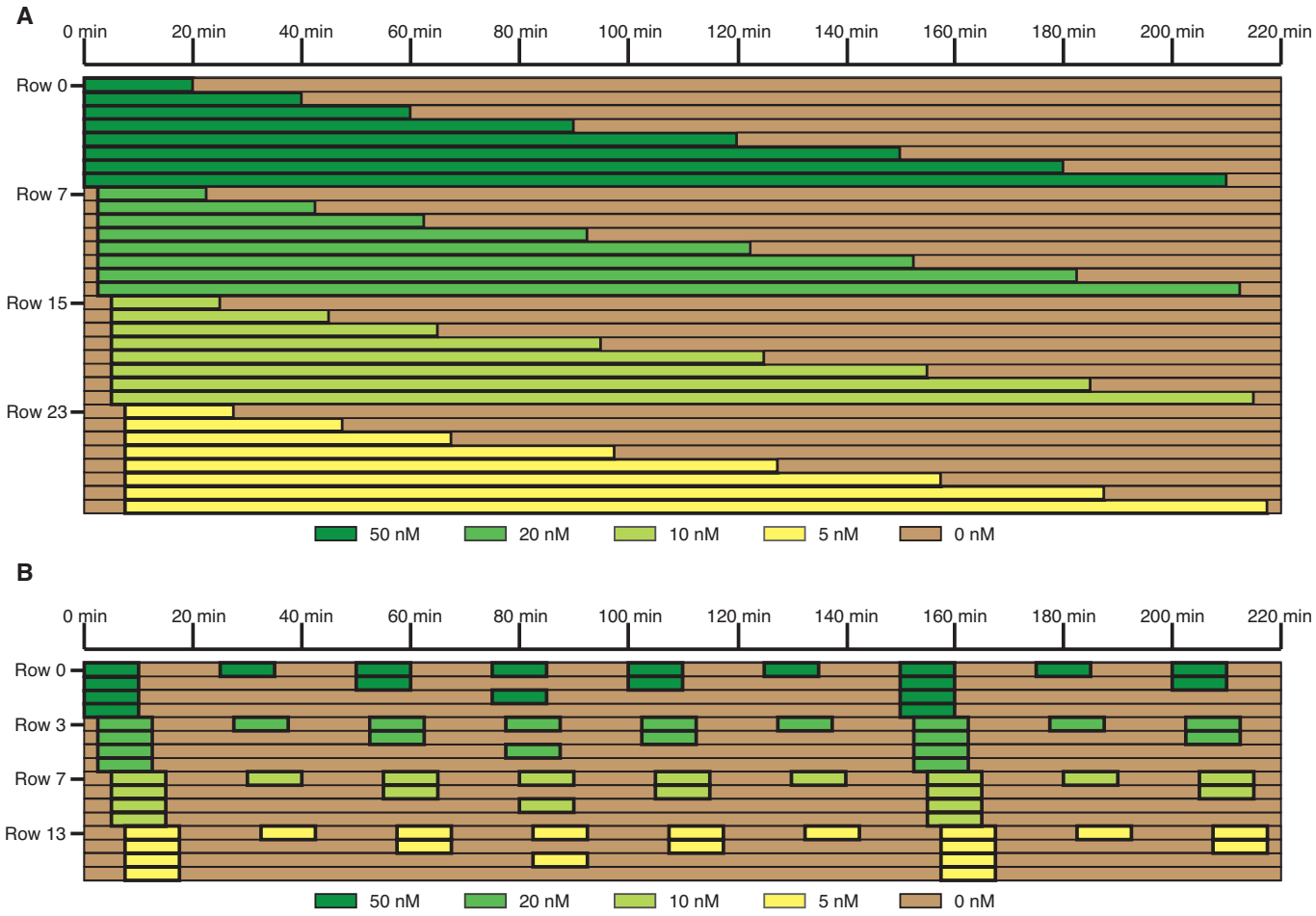

Fig. S4. Stimulation protocols. (*A*) Single-pulse experiments. Color indicates the administered α-factor concentration. Rows indicate the experimental rows in the microfluidic matrix. Horizontal axis is elapsed time. (*B*) Repeated-pulse experiments. Color indicates the administered α-factor concentration. Rows indicate the experimental rows in the microfluidic matrix. Horizontal axis is elapsed time.

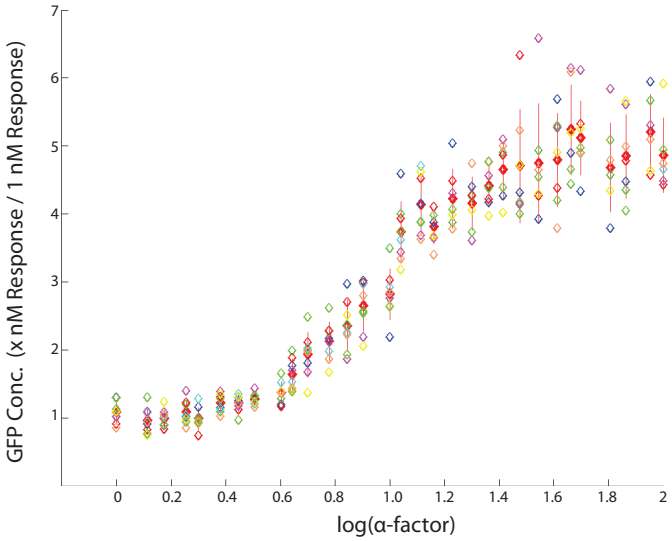

Fig. S5. Response variability within a single microfluidic device. Each data point is the steady-state population-averaged GFP concentration normalized by response to 1 nM α-factor (*y* axis) for a given α-factor concentration (*x* axis). Each microfluidic column contains the same WT genotype, with each dot color representing a different column. Red dots and lines represent the mean and SD response of all columns. Cases where an experimental position contained zero cells were removed in this analysis.

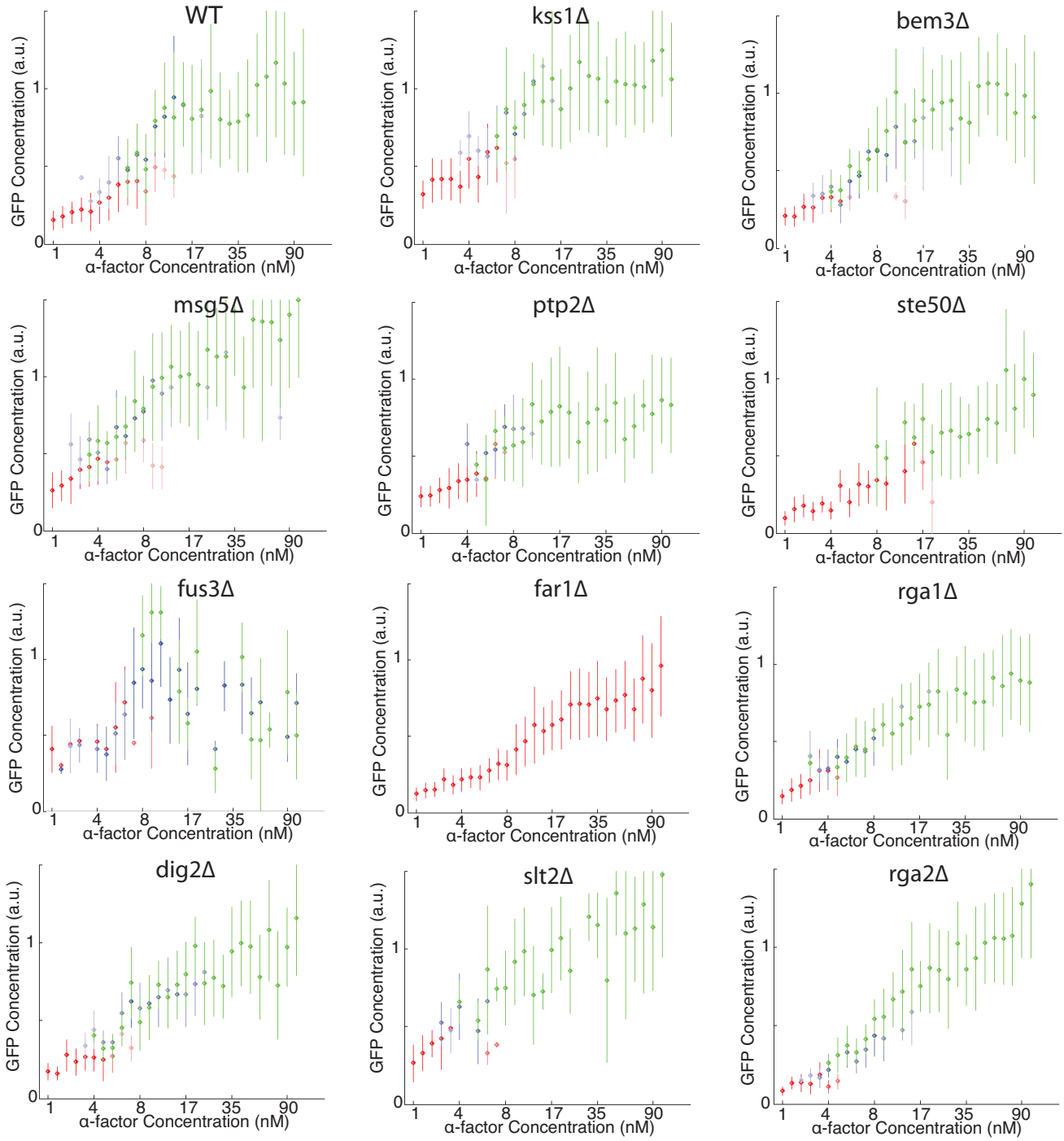

Fig. S6. Morphological response of the yeast strains to α-factor concentration. Colored dots represent morphologically stratified population mean GFP response, with dot opacity indicating the percentage of cells with that morphology for the specific experiment. Red, yeast form; blue, hyperelongated; green, shmoo. Error bars represent SD of response. Measurements were taken from the $t = 360$-min time point for all strains except *fus3*Δ, which was taken at $t = 600$ min. Mating morphologies in *fus3*Δ we not observable until this time.

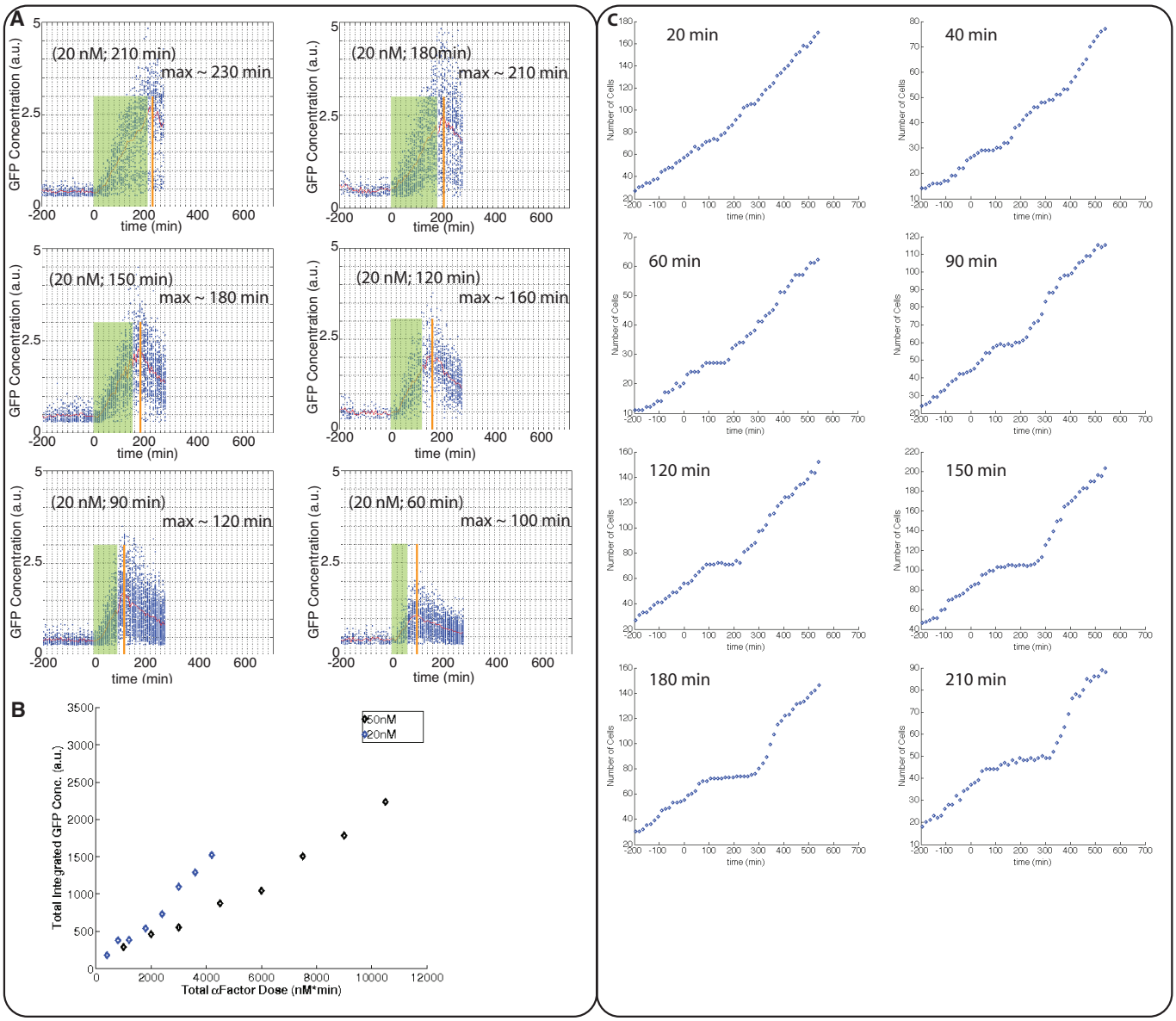

Fig. S7. Single-pulse analysis. (*A*) Time to reach maximal GFP concentration after α-factor release. The green bar indicates α-factor stimulation. The orange line indicates approximate time of GFP concentration maximum. A higher image acquisition rate of every 7.5 min was used to increase the accuracy of peak finding. (*B*) Total integrated GFP out vs. total integrated α-factor input for WT yeast. Dot color represents different input α-factor concentration: black, 50 nM; blue, 20 nM. (*C*) Growth curves of WT cells stimulated with a single 50 nM α-factor pulse. Pulse duration: 20 min; 40 min; 60 min; 90 min; 120 min; 150 min; 180 min; 210 min. α-Factor stimulation was initiated at $t = 0$. Yeast cell proliferation arrests upon stimulation with α-factor and resumes when the α-factor is washed out.

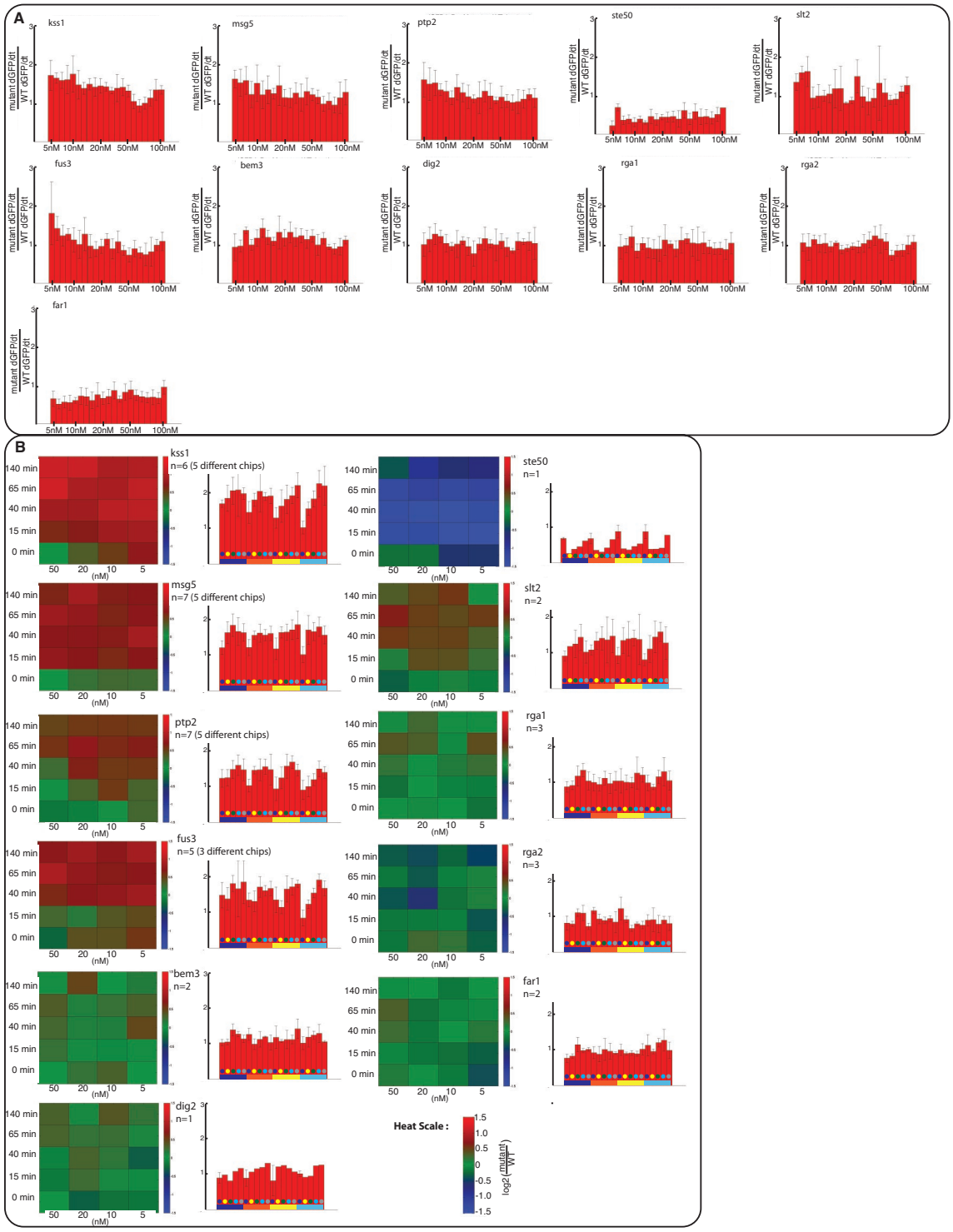

Fig. S8. Reproducibility of results. (*A*) dGFP/dt measurements. Each bar plot gives the mutant initial dGFP/dt over WT initial dGFP/dt across all α-factor concentrations between 5 and 100 nM. Initial dGFP/dt is calculated as the slope of a line fitted to the population-averaged GFP concentrations between 30 and 180 min. Error bars give SD across experiments ($n = 2$–5). (*B*) Periodic α-factor stimulation for all mutants. Heat plots and bar plots of mutant GFP concentrations vs. WT are given for all tested strains. Heat plot scales are in log2(mutant/WT), and the bar plots are in (mutant/WT). In both cases, response is taken at $t = 600$ min and averaged across n experiments (n is indicated for each strain). Error bars on the bar plot represent the SD of the measurement across experimental replicates. Number of replicates is given for each strain. If replicates from the same chip were considered, the total number of replicates from different chips is indicated. Each colored rectangle of the heat plots corresponds to a specific α-factor concentration (column) and delay between successive pulses (row). Experimental conditions of the bars of the bar plot are indicated by the colored base bar (dark blue, 5 nM; orange, 10 nM; yellow, 20 nM; light blue, 50 nM) and colored dot (dark blue, constant stimulation; yellow, 15-min delay; green, 40-min delay; light blue, 65-min delay; gray, 140-min delay).

Table S1. Pumping protocol for creating 32 different α-factor concentrations

Row	1.16^i	Used, nm	0 nM	1 nM	10 nM	100 nM
0	1	0	10	0	0	0
1	1.16	1	0	10	0	0
2	1.35	1.3	6	3	1	0
3	1.56	1.5	4	5	1	0
4	1.81	1.8	1	8	1	0
5	2.10	2	8	0	2	0
6	2.43	2.4	4	4	2	0
7	2.82	2.8	0	8	2	0
8	3.27	3.2	5	2	3	0
9	3.80	4	6	0	4	0
10	4.41	4.4	2	4	4	0
11	5.12	5	5	0	5	0
12	5.94	6	4	0	6	0
13	6.89	7	3	0	7	0
14	7.99	8	2	0	8	0
15	9.27	9	1	0	9	0
16	10.75	10	0	0	10	0
17	12.46	12.5	2	5	2	1
18	14.46	14.5	0	5	4	1
19	16.78	17	2	0	7	1
20	19.46	20	8	0	0	2
21	22.57	22.5	1	5	2	2
22	26.19	26	2	0	6	2
23	30.38	30	7	0	0	3
24	35.24	35	2	0	5	3
25	40.87	41	5	0	1	4
26	47.41	46	0	0	6	4
27	55.00	50	5	0	0	5
28	63.80	64	0	0	4	6
29	74.01	73	0	0	3	7
30	85.85	90	1	0	0	9
31	99.60	100	0	0	0	10

The first column is the row index. The second column is the exponentially calculated α-factor concentration. The third column is the actual α-factor concentration used. The final four columns are in units of number of pumps for a 10-pump cycle.

Table S2. Strains used in this study

Identifier	Genotype
WT	*MATa leu2Δ0 met15Δ0 ura3Δ0 bar1*Δ::HphNT2 *his3*::PRE-GFP-*HIS3*
*Bem3*Δ	*MATa leu2Δ0 met15Δ0 ura3Δ0 bar1*Δ::HphNT2 *his3*::PRE-GFP-*HIS3 bem3*Δ::KanMX4
*Dig2*Δ	*MATa leu2Δ0 met15Δ0 ura3Δ0 bar1*Δ::HphNT2 *his3*::PRE-GFP-*HIS3 dig2*Δ::KanMX4
*far1*Δ	*MATa leu2Δ0 met15Δ0 ura3Δ0 bar1*Δ::HphNT2 *his3*::PRE-GFP-*HIS3 far1*Δ::KanMX4
*fus3*Δ	*MATa leu2Δ0 met15Δ0 ura3Δ0 bar1*Δ::HphNT2 *his3*::PRE-GFP-*HIS3 fus3*Δ::KanMX4
*kss1*Δ	*MATa leu2Δ0 met15Δ0 ura3Δ0 bar1*Δ::HphNT2 *his3*::PRE-GFP-*HIS3 kss1*Δ::KanMX4
*msg5*Δ	*MATa leu2Δ0 met15Δ0 ura3Δ0 bar1*Δ::HphNT2 *his3*::PRE-GFP-*HIS3 msg5*Δ::KanMX4
*Ptp2*Δ	*MATa leu2Δ0 met15Δ0 ura3Δ0 bar1*Δ::HphNT2 *his3*::PRE-GFP-*HIS3 ptp2*Δ::KanMX4
*rga1*Δ	*MATa leu2Δ0 met15Δ0 ura3Δ0 bar1*Δ::HphNT2 *his3*::PRE-GFP-*HIS3 rga1*Δ::KanMX4
*rga2*Δ	*MATa leu2Δ0 met15Δ0 ura3Δ0 bar1*Δ::HphNT2 *his3*::PRE-GFP-*HIS3 rga2*Δ::KanMX4
*slt2*Δ	*MATa leu2Δ0 met15Δ0 ura3Δ0 bar1*Δ::HphNT2 *his3*::PRE-GFP-*HIS3 slt2*Δ::KanMX4
*ste50*Δ	*MATa leu2Δ0 met15Δ0 ura3Δ0 bar1*Δ::HphNT2 *his3*::PRE-GFP-*HIS3 ste50*Δ::KanMX4